Li and group-III impurity doping in $ZnSnN_2$: Potential and limitations

Vegard Skiftestad Olsen,[1,*] Ymir Kalmann Frodason,[1] Ylva Knausgaard Hommedal,[1] Dina Marie Nielsen,[1] Philip Michael Weiser,[1] Klaus Magnus Haaland Johansen,[1] In-Hwan Lee,[2] Andrej Yu Kuznetsov,[1] and Lasse Vines[1]

[1]*Department of Physics, Centre for Materials Science and Nanotechnology, University of Oslo, P.O. Box 1048, Blindern, N-0316 Oslo, Norway*

[2]*Department of Material Science and Engineering, Korea University, 02841 Seoul, Korea*

(Received 10 October 2022; revised 6 December 2022; accepted 7 December 2022; published 26 December 2022)

II–IV nitrides and their alloys represent an earth-abundant and potentially cost-efficient alternative to the well-developed AlN-GaN-InN system. A major drawback with the II–IV nitrides is that $ZnSnN_2$, the lowest band gap material, exhibits unfavorably high carrier concentrations for as-grown, stoichiometric material, limiting the material systems potential use in applications such as solar cells and light-emitting diodes. Lithium (Li) has been suggested as a shallow acceptor defect in $ZnSnN_2$ if substituting for Zn, and hence doping with Li has been identified as a possible way to improve the electronic properties. Herein, theoretical calculations by hybrid functional density functional theory have been employed and extended to include defect complexes as well, which to this point remained unexplored. The calculations reveal that even though Li on the Zn site (the Li_{Zn}) is an acceptor, the defect may easily complex with the Li_i donor, rendering the complex neutral. Our theoretical findings are supported by a Li-doping series of $ZnSnN_2$, where a doping concentration ranging from 2.10×10^{19} cm^{-3} to 1.85×10^{20} cm^{-3} was obtained. The *n*-type carrier concentration was found to be unaffected by the doping concentration, and no systematic change in the absorption onset, probably affected by a Burstein-Moss shift, was observed. Possible group-III dopants, as have been found to yield interesting results for $ZnGeN_2$, such as In, Ga, Al, and B, have also been investigated as an alternative dopant in $ZnSnN_2$.

DOI: 10.1103/PhysRevMaterials.6.124602

I. INTRODUCTION

Ternary II–IV nitrides and their alloys show great potential for tandem solar cells, light-emitting diodes, and hydrogen production through water splitting, due to their tunable functional properties. This material system attracts considerable attention, partially due to its strong similarities to the parent material system, i.e., the AlN-InN-GaN system, where the III-nitride cation is substituted by heterovalent group-II and -IV cations. For the ternary nitride system used for band gap engineering, e.g., $Zn(Sn, Ge)N_2$ [1] or $(Zn,Mg)SnN_2$ [2], $ZnSnN_2$ exhibits the lowest band gap for this category of materials, as summarized in the review by Greenaway *et al.* [3]. In particular, $ZnSnN_2$ is of specific interest in applications of II-IV nitrides as top cell components in tandem solar cells together with silicon, as the band gap is close to the optimum for the top cell.

The main challenge with stoichiometric, undoped $ZnSnN_2$ as a functional semiconductor is the unfavorably high as-grown electron density, typically in the range of 5×10^{19} cm^{-3}–5×10^{20} cm^{-3}. In addition to hindering diode fabrication, the high carrier density complicates the determination of the optical band gap due to the Burstein-Moss (BM) shift [4,5]. Both intrinsic and extrinsic defects have been identified as probable contributors to the unintentional degeneracy. The tin-zinc antisite (Sn_{Zn}), the nitrogen vacancy (V_N), and the zinc interstitial (Zn_i), listed following the trend of increasing formation energy, all act as shallow donors in $ZnSnN_2$ [6,7]. Furthermore, extrinsic impurities such as oxygen substituting for nitrogen (O_N) and hydrogen, both substitutionally and interstitially coordinated (H_N and H_i, respectively) are all typical shallow donor impurities contributing to the high carrier density in $ZnSnN_2$ [6,7].

Attempts to reduce the carrier density in $ZnSnN_2$ have been performed by nonstoichiometric growth, increasing the Zn/Sn ratio on the cation sublattice, effectively increasing the concentration of Zn_{Sn} acceptors and reducing the number of Sn_{Zn} donors [8]. Furthermore, by growing nonstoichiometric films in a nitrogen-hydrogen atmosphere followed by a postgrowth annealing step, Fioretti *et al.* reduced the carrier density to below 1×10^{17} cm^{-3} [9], following the principles of *p*-type GaN [10].

Impurity doping is another route towards electrical control, and the alkali metals have been investigated as possible acceptor dopants in $ZnSnN_2$ employing computational methods. Lithium (Li) has been identified as a shallow acceptor when substituting for Zn (Li_{Zn}), while if placed on an interstitial site, Li acts as a donor (Li_i) [7,11,12]. Notably, Li has been extensively investigated experimentally as a potential shallow acceptor in oxide semiconductors, e.g., ZnO [13,14] and NiO [15], substituting the cations. Recently, Chinnakutti *et al.* claimed to have successfully converted $ZnSnN_2$ from *n*-type conduction to *p* type by Li doping, reporting a hole concentration in the range of 9.47×10^{19} cm^{-3}–1.14×10^{20} cm^{-3} [16]. In addition, beyond the alkali metals mentioned acting

*v.s.olsen@smn.uio.no

 ©2022 American Physical Society

as acceptors if substituted for Zn in $ZnSnN_2$, elements such as boron (B), aluminum (Al), gallium (Ga), and indium (In) are expected to form acceptor defects if substituting Ge in $ZnGeN_2$, possibly limited by self-compensation [17]. There are, on the other hand, no literature data on how these impurities may act if substituting for Sn in $ZnSnN_2$.

In the present work we performed (i) in-depth theoretical investigations of Li as dopant in $ZnSnN_2$, (ii) systematic simulations for several group-III dopants in the quest for shallow acceptor defects that can suppress the as-grown carrier density and possibly enable *p*-type conduction in $ZnSnN_2$, and (iii) a comparison with experimental data on the epitaxially grown $ZnSnN_2$ doped with Li. The series of thin films were grown with different Li contents in order to examine the impact of shallow acceptor doping on the electrical carrier density in the material. Moreover, an undoped $ZnSnN_2$ layer was capped with Li-doped $ZnSnN_2$, acting as a Li reservoir, to study the diffusion in $ZnSnN_2$.

II. METHODOLOGY

A. Computational details

$ZnSnN_2$ exhibits a low cation order-disorder transition temperature [18]. However, previous calculations have shown that the defect properties are mainly determined by the local coordination environment [7]. Therefore, we have used only the ordered $Pna2_1$ orthorhombic structure for our theoretical investigation of impurities.

All first-principles calculations were performed within the framework of the generalized Kohn-Sham theory, using projector-augmented wave potentials [19,20], as implemented in VASP [21]. The Ga 3*d*, In 3*d*, and Li 1*s* electrons were included explicitly as valence electrons. Unless otherwise specified, we employed the screened hybrid functional of Heyd, Scuseria and Ernzerhof (HSE06) [22]. Following Tsunoda *et al.* [7], the mixing parameter α is kept at the standard value of 0.25, yielding lattice parameters ($a = 6.75$ Å, $b = 5.85$ Å, and $c = 5.47$ Å) in good agreement with experiment [23], and a direct band gap value of 1.41 eV. In Ref. [7], a BM shift of 0.2–0.3 eV was calculated for carrier concentrations in the 10^{18}–10^{21} cm^{-3} range as typically observed in grown films. Indeed, a band gap in the range of 1.61–1.71 eV is in good agreement with our epitaxially grown $ZnSnN_2$ [24].

Calculations for defects in $ZnSnN_2$ were performed using a 128-atom orthorhombic supercell. We used a single special *k* point at (0.25,0.25,0.25) to sample the Brillouin zone, and a 400-eV cutoff energy for the plane-wave basis set. Formation energies and thermodynamic charge-state transition levels were evaluated using the standard formalism described in Ref. [25]. For example, the formation energy of Al_{Sn} in charge state q is given by

$$E^{f}(Al^{q}_{Sn}) = E_{tot}(Al^{q}_{Sn}) - E_{tot}(ZnSnN_2) + \mu_{Sn} - \mu_{Al} + q(\varepsilon_{VBM} + \Delta\varepsilon_F), \quad (1)$$

where $E_{tot}[Al^{q}_{Sn}]$ and $E_{tot}[ZnSnN_2]$ are the total energies of the supercell containing Al_{Sn} and the pristine supercell, respectively. The added and removed Al and Sn atoms are exchanged with reservoirs of chemical potential μ_{Al} and μ_{Sn}, respectively. Electrons are similarly exchanged with the Fermi level, which is given with respect to the valence band maximum: $\varepsilon_F = \varepsilon_{VBM} + \Delta\varepsilon_F$. The chemical potentials of host and impurity atoms considered here are referenced to the following competing phases: Zn, Sn, N_2, Li, BN, AlN, GaN, In, and H_2. Owing to the small heat of formation (ΔH_f) of $ZnSnN_2$ [7,11], formation energies are presented only for chemical potentials corresponding to the condition of $ZnSnN_2$ in equilibrium with metal Zn and Sn [7], i.e., $\Delta\mu_{Zn} = \Delta\mu_{Sn} = 0$ and $\Delta\mu_N = \frac{1}{2}\Delta H_f(ZnSnN_2)$. For charged defects, the first term in Eq. (1) includes a finite-size correction, calculated by following the scheme in Refs. [26,27].

Defect migration barriers were determined using the climbing-image nudged elastic band (NEB) method [28], using 7–11 images between end-point defect structures. For each image, forces acting in the direction perpendicular to the path were converged to within 50 meV/Å. The NEB calculations were performed using the strongly constrained and appropriately normed (SCAN) functional [29], keeping the lattice parameters fixed to those obtained using HSE06 (close to experimental values).

B. Experimental details

The $ZnSnN_2$ thin films were grown using Polyteknik Flextura magnetron sputter cluster equipment, with a base pressure lower than 2×10^{-8} mbar. Three separate 3″ metallic targets were employed to fabricate the samples, namely, a Zn (99.995%), a Li-doped Zn (99.95%) with Li concentration of 1 wt %, and a Sn (99.999%) target. The reactive sputtering process was conducted in a mixture of Ar and N_2 gas at a process pressure of 2×10^{-3} mbar. The substrate temperature and rotation were kept at 350 °C and 10 rpm, respectively. In order to stabilize the substrate temperature, an *in situ* annealing at 350 °C was conducted for 30 min prior to deposition. The Zn target was placed at the HiPIMS source, whereas Li-doped Zn and Sn targets were mounted on conventional rf magnetron sputtering sources. The applied target powers were adjusted between each deposition to obtain different Li-doping concentrations, while still ensuring a stoichiometric relationship between the cations, i.e., Zn/(Zn + Sn) = 0.5 (see Table II). For the HiPIMS source, the frequency was optimized to 1400 Hz.

Compositional analysis was undertaken employing secondary electron microscopy energy dispersive x-ray spectroscopy (SEM EDS). SEM EDS measurements were conducted on a JEOL IT-300 instrument equipped with a Thermo Fisher Ultradry EDS detector. Quantification results are based on standardless phi-rho-Z analysis, with data captured using 12 kV accelerating voltage, 20% detector dead time at 108 600 cps.

Secondary ion mass spectrometry (SIMS) mass spectra and depth profiles were obtained using a Cameca IMS 7f microanalyzer with either 15 keV Cs^+ or 10 keV $O_2{}^+$ as primary ions. The depth of the sputtered crater was measured by a Veeco Dektak 8 stylus profilometer. Assuming a uniform and time-independent erosion rate, the measured crater depth was used to convert sputtering time to the crater depth.

X-ray diffraction (XRD) was utilized for structural characterization. A Bruker AXS D8 Discover system was employed. The x-ray source was Cu $K\alpha$ ($\lambda = 1.5406$ Å), and a Ge (220)

double bounce monochromator was implemented to filter out the $K\alpha_2$ signal ($\lambda = 1.5444$ Å). The instrumental broadening of the diffraction peaks of 0.008° is included in the standard error of the values given.

Optical absorption properties of the films were derived from the transmittance measurements performed at room temperature using a Shimadzu SolidSpe-3700 DUV UV-Vis spectrophotometer with 0.1 nm spectral resolution. A measurement of an empty sample holder was used as a background measurement. Transmittance measurements were also conducted at room temperature using a Bruker IFS 125HR Fourier transform spectrometer equipped with a DLaTGS detector. Measurements in the mid- (near-) infrared region utilized a globar (tungsten) source and a KBr (CaF_2) beamsplitter. Transmittance of light through the empty sample holder was used for the background single-channel spectrum, and all measurements were performed with the light at normal incidence (+/− °) to the thin film. All experiments used a spectral resolution of 4 cm^{-1}. The room-temperature Hall-effect measurements were undertaken using a Lake Shore 7604 EM4 HGA instrument. The room-temperature measurements were variable field measurements, with the magnetic field varied from 1 kG to 10 kG in steps of 1 kG. Contacts were soldered onto the sample using In. A voltage tracking measurement was conducted prior to each variable field measurement to ensure reliable results.

The $ZnSnN_2$ thin films were grown on 500-μm-thick single-crystal (0002) ZnO commercial substrates, following the same process as reported in Olsen *et al.* [24]. Prior to the growth, the O-face (000$\bar{2}$) was box implanted with P^+ ions in order to fabricate a highly resistive surface layer to enable subsequent reliable electrical characterization of the $ZnSnN_2$ film. The substrates were implanted with P ions in two steps: (i) to a dose of 2×10^{14} cm^{-3} with an energy of 36 keV, and (ii) to a dose of 2×10^{14} cm^{-3} with an energy of 180 keV. After implantation, the substrates were cleaned in acetone, isopropanol, and deionized water, dried in N_2 flow and annealed in O_2 atmosphere at 800 °C for 1 h to recover structural damages caused by the implantation step, and prepare a substrate surface suited for epitaxial growth. In between characterization steps, all films were contained in a nitrogen atmosphere to minimize the oxidation effects.

III. RESULTS AND DISCUSSION

A. Li configurations and migration in $ZnSnN_2$

Figure 1 shows the formation energy of Li impurity-related defects (Li_{Zn}, Li_i, and complexes), as well as the intrinsic defects previously shown to be the dominant donor (Sn_{Zn}) and acceptor (Zn_{Sn}) in $ZnSnN_2$ [6,7]. Li_{Sn} and Li_N are omitted, as the former exhibits very high formation energy and the latter is found to be unstable.

Previous hybrid functional studies by Wang *et al.* [11] and Tsunoda *et al.* [7] point to Li as the only shallow acceptor among the alkali metals substituted on the Zn site. Indeed, the neutral charge states of the deep Na_{Zn} and K_{Zn} acceptors correspond to a small hole polaron localized at one of the N ions immediately adjacent to the impurity, whereas a delocalized

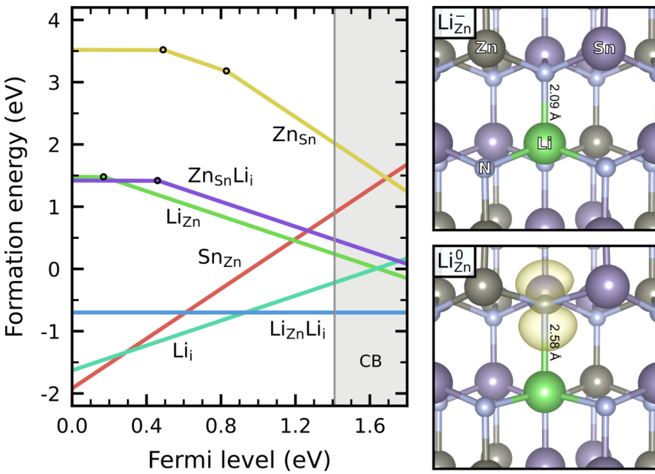

FIG. 1. Left: Formation energy as a function of Fermi level relative to the VBM for native defects (Sn_{Zn} and Zn_{Sn}), Li impurities (Li_{Zn}, Li_{Sn}, Li_i), and complexes involving Li impurities ($Li_{Zn}Li_i$ and $Zn_{Sn}Li_i$). Right: Relaxed structure of Li^-_{Zn}, and of Li^0_{Zn} with the hole (yellow isosurface) localized in a polaronic state at the axial N ion.

perturbed host state was found for Li_{Zn} [7,11]. In the present work, however, we find a deep polaronic ground state also for the Li_{Zn} acceptor. We note that a large displacement of Li had to be introduced before ionic relaxation in order to find this state. The relaxed structure in Fig. 1 shows the hole localized at the axial N ion, and the axial Li-N bond is elongated by 23% with respect to the corresponding bond length for Li_{Zn} in the negative charge state. In contrast, Na and K reside close to the ideal Zn site for both charge states [7]. This result is similar to what has been found for these impurities in ZnO [30].

Despite the deep ground state, the corresponding $\varepsilon(0/-)$ level of Li_{Zn} is located only 0.17 eV above the valence band maximum (VBM). The deep and shallow states are thus close in energy, similar to the dual behavior previously reported for the Mg_{Ga} and Be_{Ga} acceptors in GaN [31,32]. Hence, the present results suggest that Li_{Zn} can be a moderately effective *p*-type dopant in $ZnSnN_2$.

However, in agreement with previous calculations by Tsunoda *et al.* [7], we find that the Li_i donor is the most stable configuration of the Li impurity for all Fermi-level positions in the band gap. The crossing point between the formation energies of the Li_i donor and the Li_{Zn} acceptor occurs 0.2 eV above the conduction band minimum (CBM), limiting the *n*-type doping efficiency. The position of this crossing point is indeed approximately invariant to the choice of chemical potential in our calculations, due to the low ΔH_f of $ZnSnN_2$, as described in Sec. II A. However, Wang *et al.* [11] have questioned the role of Li_i as a thermally stable donor due to the expectation of a low migration barrier. In this case, Li_i donors should be easily removed by a postgrowth annealing step, similar to hydrogen [9]. The mobility of Li_i is therefore central to understanding the electrical behavior of Li. For this reason, we have performed NEB calculations to determine the minimum energy paths for migration of Li_i^+.

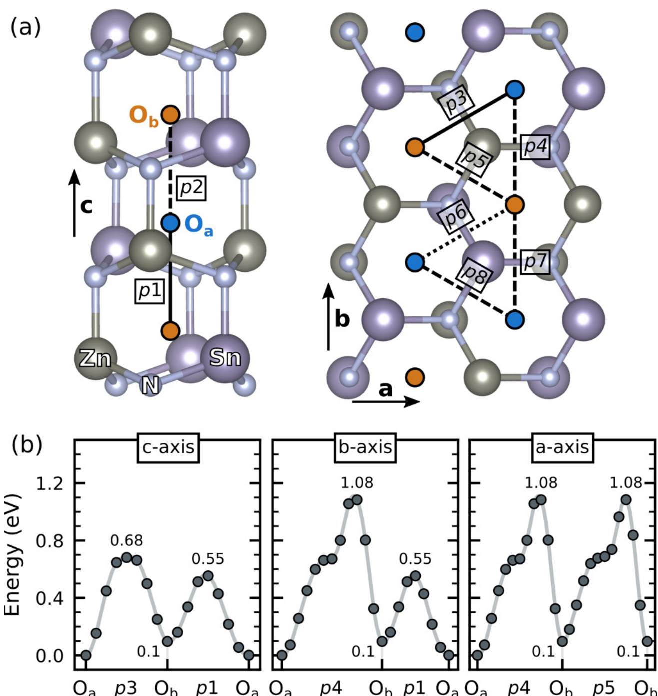

FIG. 2. (a) Possible migration paths $p1$–$p8$ between different nearest-neighbor octahedral interstitial sites O_a (blue) and O_b (orange) in the ordered $ZnSnN_2$ structure. (b) Minimum energy paths for Li_i migration along the c, b, and a axes.

Figure 2(a) shows eight crystallographically inequivalent paths ($p1$–$p8$) between octahedral interstitial sites in the ordered $Pna2_1$ structure of $ZnSnN_2$. There are two distinct octahedral interstitial sites (labeled O_a and O_b), which differ by the arrangement of the six nearest-neighbor Zn and Sn ions. Li_i prefers the O_a site, which has one Sn and two Zn ions in the nearest of the two Zn/Sn layers (two Sn and one Zn in the other layer), but the O_b site is merely 0.1 eV higher in energy. The tetrahedral interstitial sites are found to be significantly higher in energy and/or unstable. Table I lists the calculated migration barriers for the $p1$–$p8$ paths.

For Li_i^+ migration through the open hexagonal channel along the c axis, the impurity must sequentially pass through a triangle of N ions and Zn/Sn ions. For migration in directions perpendicular to the c axis, we find that the Li ion prefers to move through a tetrahedral interstitial site, which similarly requires passing through two Zn/Sn triangles. The magnitude of the migration barrier is found to correlate with the motif of the Zn/Sn triangle, with $ZnSn_2$ yielding significantly higher barriers than Zn_2Sn, i.e., the barrier for path $p1$ and $p2$ is 0.68 and 1.31 eV, respectively. This is likely related to the larger ionic radius of Sn compared to Zn. For migration along the c axis, the minimum-energy path will therefore not run straight along the axis. As shown in Fig. 2(b), migration along the c axis will rather proceed via the $p1$ and $p3$ paths which only require crossing Zn_2Sn triangles, yielding a low overall barrier of 0.68 eV. Conversely, for long-range migration along the a axis and b axis, crossing a $ZnSn_2$ triangle cannot be avoided, yielding a significantly higher barrier of 1.08 eV for both directions.

The temperature at which Li_i^+ diffusion becomes experimentally measurable can be estimated from harmonic transition state theory, where the transition rate is given by $\Gamma = \Gamma_0 \exp(-E_m/k_B T)$. If Γ is set to one jump per second, and a typical phonon frequency of 10^{13} s^{-1} is used for the attempt frequency Γ_0, the annealing temperature is given by $T_a = E_m \times 388$ K/eV [33]. This means Li_i^+ will start diffusing at about 260 and 420 K for directions parallel and perpendicular to the c axis, respectively. Thus, Li_i^+ will diffuse in any direction at the 350 °C growth temperature, and along the c axis at room temperature.

However, the minimum-energy paths determined from the analysis above are only valid for the ordered structure. The low barrier of 0.68 eV for migration along the c axis relies on having an uninterrupted pathway of Zn_2Sn-type jumps, which is perhaps less likely in a disordered structure. Li_i^+ is nonetheless expected to be mobile at the growth temperature. Another possibility is that Li_i^+ is bound in a more thermally stable configuration. For example, a disordered structure presents additional types of octahedral interstitial sites that could be more favorable, and serve as trapping sites for Li_i. Moreover, the Li_i^+ donor is likely to form complexes with and thus passivate acceptor defects such as Li_{Zn} (self-passivation) or Zn_{Sn} (see Fig. 1). The binding energy of these complexes can be calculated as the difference in formation energy between the complex and the sum of the formation energies of Li_i and the acceptor. We obtain binding energies of 0.72 and 1.33 eV for the $Li_{Zn}Li_i$ and $Zn_{Sn}Li_i$ complexes, respectively. If the dissociation energy of these complexes is estimated as the sum of the binding energy and the lowest migration barrier of 0.68 eV, the dissociation temperature should be at least 540 and 780 K. Thus, the temperature required in a postgrowth annealing step to remove Li_i donors and activate the acceptors could pose a challenge. In particular considering the low thermal stability of $ZnSnN_2$.

TABLE I. Migration barrier for paths $p1$–$p8$, as obtained from NEB calculations employing the SCAN functional. For paths connecting different octahedral sites, the barrier corresponds to the transformation from O_a to O_b. The barrier for the opposite direction can be obtained by subtracting 0.1 eV. The barrier for the $p6$ path could not be determined because the images relaxed to an alternative pathway ($p8 + p7$).

	$p1$	$p2$	$p3$	$p4$	$p5$	$p6$	$p7$	$p8$
E_m (eV)	0.55	1.31	0.68	1.08	0.99		1.46	1.43

B. Energetics of group-III dopants in $ZnSnN_2$

Using hybrid functional calculations, we have also assessed the group-III impurities B, Al, Ga, and In as candidate acceptor dopants. These were previously investigated by Adamski *et al.* [17] for $ZnGeN_2$, and found to be promising acceptor dopants. As trivalent impurities, they are expected to behave as single donors and acceptors when incorporated on the Zn and Sn sites, respectively. Figure 3 shows the calculated formation energy for each impurity in both of these configurations.

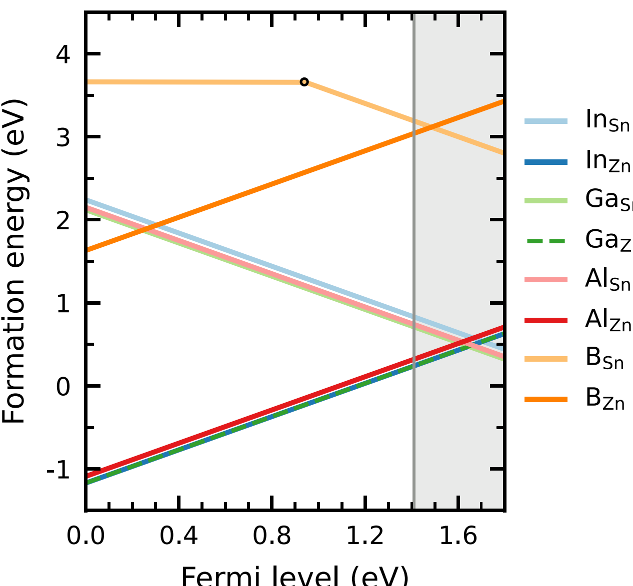

FIG. 3. Formation energy as a function of Fermi level relative to the VBM for group-III impurities (B, Al, Ga, and In) substituting on the Zn or Sn sites in $ZnSnN_2$.

In contrast to Li_{Zn}, we find that Al_{Sn}, Ga_{Sn}, and In_{Sn} behave as shallow acceptors, i.e., no deep polaronic state could be stabilized. For the B_{Sn} acceptor, however, we find a very deep $\varepsilon(0/-)$ level located 0.94 eV above the VBM. This is likely related to its small ionic radius compared to the other impurities. Indeed, in the neutral charge state of B_{Sn}, the B atom moves off the ideal Sn site, forming bonds with three N ions, and a hole polaron is strongly bound at the N ion with a dangling bond.

Although Al_{Sn}, Ga_{Sn}, and In_{Sn} behave as shallow acceptors, we find that all of the group-III impurities prefer to form shallow donors on the Zn site for all Fermi-level positions within the band gap. The pinning levels (crossing points between the acceptor and donor configurations) are located 0.1–0.3 eV above the CBM, similar to Li. Self-compensation due to wrong-site occupation is therefore a bigger obstacle to overcome for these impurities in $ZnSnN_2$ compared to in $ZnGeN_2$, where the pinning level was reported to be around midgap [17]. Also, in contrast to Li, where the donor configuration is a relatively mobile interstitial, the Al_{Zn}, Ga_{Zn}, and In_{Zn} donors are more likely to be immobile at relevant temperatures.

C. Structural, electrical, and optical data from Li-doped $ZnSnN_2$

Extending our theoretical results pointing towards issues with Li acceptors in $ZnSnN_2$ due to the formation of neutral and stable defect complexes with interstitial Li and H, we fabricated highly crystalline $ZnSnN_2$ thin films with varying Li content. The Li concentration in the films, as well as their growth parameters, are listed in Table II. Sample A represents an undoped $ZnSnN_2$ thin film, acting as a reference sample. From sample B to sample H, the target power applied to the Li:Zn target was increased in order to incorporate an increasing amount of Li. Notably, all samples from A–H, with the

TABLE II. Growth parameters, stoichiometry with atomic percentages measured by the SEM EDS and calculated cation-ratios, thickness data, and average Li concentration measured by SIMS.

Sample	Zn (W)	Li:Zn (W)	Sn (W)	Zn/(Zn+Sn)	Thickness (nm)	[Li] (cm^{-3})
A	44	0	36	0.51	471	
B	40	8	36	0.42	400	4.02×10^{19}
C	36	12	36	0.51	426	2.10×10^{19}
D	36	16	36	0.51	496	3.25×10^{19}
E	26	26	36	0.52	465	1.07×10^{20}
F	20	32	36	0.52	533	1.47×10^{20}
G	16	38	36	0.52	429	1.85×10^{20}
H	0	44	36	0.57	671	1.68×10^{20}

exceptions of B and H, are stoichiometric, meaning that the $Zn/(Zn + Sn)$ ratio is equal or close to 0.5. Samples B and H are Sn rich and Zn rich, respectively, and any analysis on these samples should therefore be done keeping this fact in mind. Indeed, the nonstoichiometry has proven to be an efficient method to alter the optoelectronic properties of $ZnSnN_2$ [8,9].

Figure 4 shows the Li concentration ([Li]) vs depth profiles of Li in all samples, where sample A can clearly be distinguished as having a low Li concentration. In fact, the measured [Li] in sample A ($\sim 2 \times 10^{14}$ cm^{-3}) is close to the detection limit of SIMS. For the rest of the samples, the doping profiles are uniform as a function of depth, except of samples E and F, yielding slightly higher [Li] closer to the thin film surface. The Li incorporation increases with the samples ID, and as seen from the inset in Fig. 4, the [Li] increases with applied Li:Zn target power, as may be expected. Thus, the doping was successfully undertaken covering [Li] from $\sim 2 \times 10^{19}$ cm^{-3} to $\sim 2 \times 10^{21}$ cm^{-3}.

To ensure that the structural properties of the $ZnSnN_2$ films remained satisfactorily high [24], as well as to examine any

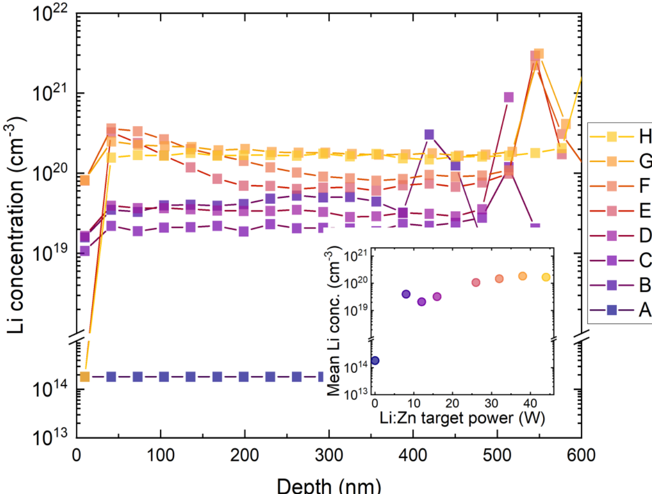

FIG. 4. SIMS depth profiles of the Li content in the $ZnSnN_2$ thin films. The last measurement point before the following intense peak for each sample (above depths of 400 nm) represents the thin film–substrate interface. The inset shows the calculated average in Li concentration of the different samples as a function of applied Li:Zn target power.

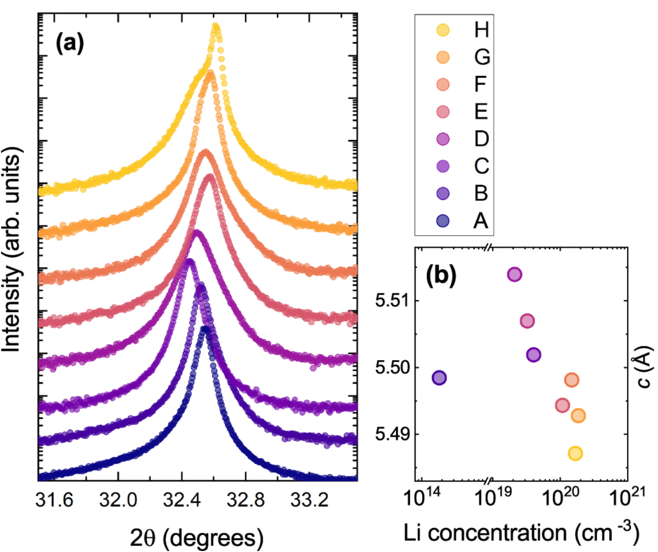

FIG. 5. Locked-couple ($\theta-2\theta$) scans of the (0002) reflections as a function of Li concentration (samples A–H).

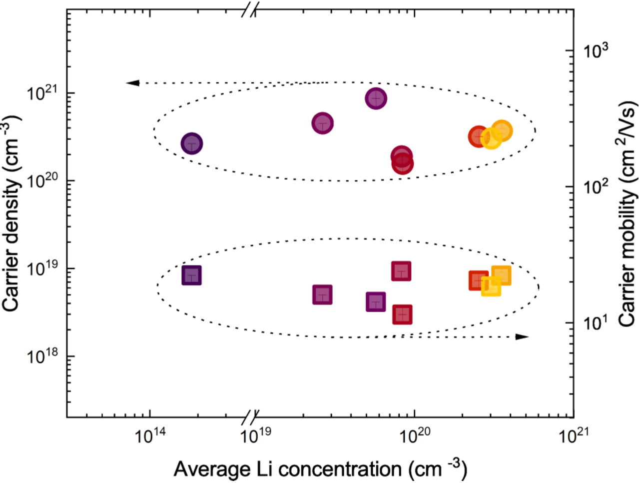

FIG. 6. Room-temperature Hall-effect measurements as a function of average Li concentration. The left y axis shows the carrier density for the circle data points, whereas the right y axis and square data points represents the carrier mobility.

potential phase transformation upon doping, we performed systematic XRD measurements (see Fig. 5 and additional data in the Supplemental Material [34]). Importantly, there is no evidence supporting the presence of any LiN phase, e.g., the $\alpha-Li_3N$ phase (space group 191, $P6/mmm$) [35]. Focusing on the (0002) reflection and its dependence on Li incorporation [as shown in Fig. 5(a)], the reflection remains one distinct peak until sample F; after that, in samples G and H, a lower-angle shoulder emerges. This shoulder becomes more prominent in the highest Li-containing sample (sample H), indicating that Li incorporation is responsible for the evolution. The peak maximum for the (0002) $ZnSnN_2$ reflection moves first towards lower angles from sample A to sample C, after which the evolution of the (0002) peak position turns and shifts towards higher angles [see Fig. 5(a)]. Sample H has its peak maximum at $2\theta = 32.61^\circ$, which may be compared to the undoped sample (A) that exhibits peak maximum at $2\theta = 32.54^\circ$.

Figure 5(b) plots the c-lattice constant as calculated from the (0002) peak position for all samples, as a function of [Li] extracted from Table II, confirming a systematic evolution. From the undoped sample, an expansion in the growth direction occurs upon doping, i.e., comparing the undoped sample and the lowest doping concentration (2.1×10^{19} cm^{-3}). By further increasing [Li], the c parameter is reduced, reaching a minimum for sample H (highest [Li]). A similar c-parameter dependence was observed in Li-doped ZnO, where it was argued that for low [Li], Li occupies the interstitial sites, whereas after a certain [Li] threshold, additional Li atoms replace Zn in the lattice [36].

The main purpose of doping the $ZnSnN_2$ thin films with Li was to reduce the n-type carrier concentration, n, that for undoped samples remains in the range of 10^{20}–10^{21} cm^{-3} for stoichiometric compositions [8,24], as also confirmed in this work. Hall effect measurements at room temperature were conducted to extract n and the carrier mobility, μ, as a function of Li doping (see Fig. 6). From Fig. 6 one can clearly see that the n remains higher than 1×10^{20} cm^{-3} throughout the series, and independently of [Li]. The carrier mobility varies in the range of 10–30 cm^2/V s, consistent with the literature data for highly crystalline, undoped samples [24,37]. No correlation between [Li] and n corroborates our, and previously published [7,11,12] theoretical findings, meaning that the Li_{Zn} acceptor is not the dominant configuration. Importantly, n does not increase with [Li] either, supporting the following: (i) the Fermi level is pinned at the crossing point between the Li_i donor and the Li_{Zn} acceptor, which is very close to the crossing point between the Sn_{Zn} donor and the Zn_{Sn} acceptor (see Fig. 1), and therefore does not lead to an increase in free carrier concentration; and (ii) Li forms stable electrically inactive $Li_i - Li_{Zn}$ pairs with no effect on the free-carrier concentration.

Figure 7(a) shows the absorption coefficient, α, for all samples as calculated from the optical transmission measurements. It can be seen that α does not reveal radical systematic changes with respect to [Li]. As undoped $ZnSnN_2$ is considered to be degenerate, the measured optical absorption onset (often evaluated as optical band gap of semiconductors) is most likely influenced by the BM shift [4,5], i.e., blueshift the absorption onset with respect to the true band gap value. For example, Fioretti *et al.* reported on a systematic shift in the $ZnSnN_2$ absorption onsets when increasing the nonstoichiometry, i.e., making the material more Zn rich [8,9]. The band gap of the Li-doped $ZnSnN_2$ samples was estimated by Tauc-plot analysis for direct allowed transitions, as shown in Fig. 7(b). The estimated band gap does not change significantly or systematically upon doping, i.e., no reduction in BM shift is observed, and the band gap energies agree well with previously reported literature data for undoped $ZnSnN_2$ [24]. Figure 7(a) furthermore shows that α increases at low photon energies (below 1 eV), which can be explained by free-carrier absorption in the films. The free-carrier absorption was investigated in more detail by transmission measurements in the infrared region by employing Fourier-transform infrared spectroscopy (FTIR) instrument, as can be seen in the Supplemental Material [34]. No evident reductions in the

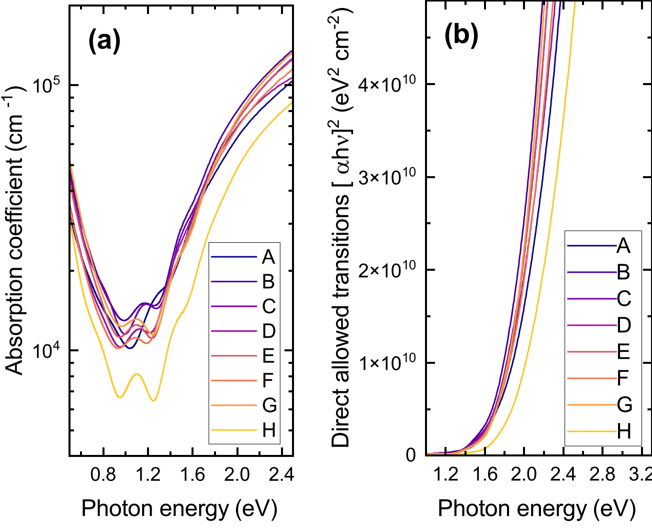

FIG. 7. Optical absorption properties of the Li-doping series. (a) shows the calculated absorption coefficient as a function of photon energy, whereas (b) shows a more classical Tauc-plot analysis to evaluate the absorption onset for direct allowed transitions.

free-carrier absorption at longer wavelengths (lower photon energies) were observed as a function of [Li] in the films. The optical data are therefore also consistent with no significant electronic response upon Li doping in $ZnSnN_2$. Postgrowth annealing to activate the Li_{Zn} acceptor by the removal of Li_i was found to require temperatures between 504 and 780 K based on our calculations, depending on the migration path of Li_i. This poses a challenge in that $ZnSnN_2$ shows low thermal stability. As an example, postgrowth annealing of $ZnSnN_2$ at 450 °C yielded loss in the preferred orientation (as shown in Fig. S3 in the Supplemental Material), i.e., the (0002) reflection is no longer the only $ZnSnN_2$-related diffraction peak.

From SIMS measurements on a $Li:ZnSnN_2/ZnSnN_2/Si$ stack (with [Li] similar to samples H/A/Si) grown *in situ*, the measured [Li] concentration was found to be as high in the undoped layer compared to the Li reservoir after deposition, as shown in Fig. S4(a) in the Supplemental Material [34]. The fact that Li has diffused from the Li reservoir ($Li:ZnSnN_2$ layer) and throughout the undoped layer during deposition corroborates our theoretically determined migration barriers of Li in $ZnSnN_2$. Indeed, Li was found to be mobile in all directions (i.e., parallel to and perpendicular to the growth direction) at the growth temperature of 350 °C employing theoretical calculations.

IV. CONCLUSIONS

We have explored potential *p*-type dopants in $ZnSnN_2$, both with hybrid functional theory and experiments. Firstly, screening of the group-III elements such as In, Ga, Al, and B were found to be inefficient acceptor dopants in $ZnSnN_2$ because of self-compensation due to wrong-site occupation. Secondly, systematic studies of Li suggest that effective *p*-type doping of $ZnSnN_2$ using Li can be challenging because (i) Li_{Zn} exhibits a relatively deep $\varepsilon(0/-)$ acceptor level located 0.17 eV above the VBM; (ii) the Li_i donor is the most stable configuration of Li for all Fermi-level positions in the band gap; and (iii) the calculated Li_i migration barriers cast doubt on whether the Li_i donor is sufficiently mobile to be efficiently removed by postgrowth annealing, especially when forming complexes with acceptors such as Li_{Zn} and Zn_{Sn} with binding energies of 0.72 and 1.33 eV, respectively. In ordered material, the lowest barrier is 0.68 and 1.08 eV for migration along and perpendicular to the *c* axis, respectively, but the former path is perhaps less likely to be available in disordered material. These calculations are supported by experimental findings, where the carrier density is found to remain independent of Li content during growth. Furthermore, the optical absorption edge also remained stable throughout the doping series. The optical band gap of the samples was measured to be consistent to undoped $ZnSnN_2$, revealing no significant change in the BM shift, corroborating the electrical findings.

ACKNOWLEDGMENTS

This work is funded by the Research Council of Norway (RCN) and is acknowledged for the support to NEARTEAMS project, Project No. 322382; the Go-POW project, Project No. 314017; and the FME Susoltech, Project No. 257639. RCN is also acknowledged for the support to UiO MiNaLab as part of the Norwegian Micro- and Nano-Fabrication Facility, NorFab, Project No. 295864. The computations were performed on resources provided by UNINETT Sigma2, the National Infrastructure for High Performance Computing and Data Storage in Norway.

[1] P. Narang, S. Chen, N. C. Coronel, S. Gul, J. Yano, L.-W. Wang, N. S. Lewis, and H. A. Atwater, Adv. Mater. **26**, 1235 (2013).
[2] N. Yamada, M. Mizutani, K. Matsuura, M. Imura, H. Murata, J. Jia, and F. Kawamura, ACS Appl. Electron. Mater. **3**, 4934 (2021).
[3] A. L. Greenaway, C. L. Melamed, M. B. Tellekamp, R. Woods-Robinson, E. S. Toberer, J. R. Neilson, and A. C. Tamboli, Annu. Rev. Mater. Res. **51**, 591 (2021).
[4] E. Burstein, Phys. Rev. **93**, 632 (1954).
[5] T. S. Moss, Proc. Phys. Soc. London Sect. B **67**, 775 (1954).
[6] S. Chen, P. Narang, H. A. Atwater, and L.-W. Wang, Adv. Mater. **26**, 311 (2013).
[7] N. Tsunoda, Y. Kumagai, A. Takahashi, and F. Oba, Phys. Rev. Appl. **10**, 011001(R) (2018).
[8] A. N. Fioretti, A. Zakutayev, H. Moutinho, C. Melamed, J. D. Perkins, A. G. Norman, M. Al-Jassim, E. S. Toberer, and A. C. Tamboli, J. Mater. Chem. C **3**, 11017 (2015).
[9] A. N. Fioretti, A. Stokes, M. R. Young, B. Gorman, E. S. Toberer, A. C. Tamboli, and A. Zakutayev, Adv. Electro. Mater. **3**, 1600544 (2017).
[10] S. Nakamura, N. Iwasa, M. Senoh, and T. Mukai, Jpn. J. Appl. Phys. **31**, 1258 (1992).
[11] T. Wang, C. Ni, and A. Janotti, Phys. Rev. B **95**, 205205 (2017).

[12] A. Bafekry, M. Faraji, M. M. Fadlallah, B. Mortazavi, A. A. Ziabari, A. B. Khatibani, C. V. Nguyen, M. Ghergherehchi, and D. Gogova, J. Phys. Chem. C **125**, 13067 (2021).
[13] L. Vines, E. V. Monakhov, R. Schifano, W. Mtangi, F. D. Auret, and B. G. Svensson, J. Appl. Phys. **107**, 103707 (2010).
[14] K. M. Johansen, A. Zubiaga, I. Makkonen, F. Tuomisto, P. T. Neuvonen, K. E. Knutsen, E. V. Monakhov, A. Y. Kuznetsov, and B. G. Svensson, Phys. Rev. B **83**, 245208 (2011).
[15] R. Karsthof, H. von Wenckstern, V. S. Olsen, and M. Grundmann, APL Mater. **8**, 121106 (2020).
[16] K. K. Chinnakutti, L. Patra, V. Panneerselvam, D. Govindarajan, S. Kheawhom, J. Theerthagiri, Y. Yu, S. T. Salammal, and M. Y. Choi, Mater. Today Chem. **25**, 100957 (2022).
[17] N. L. Adamski, Z. Zhu, D. Wickramaratne, and C. G. V. de Walle, Appl. Phys. Lett. **114**, 032101 (2019).
[18] S. Lany, A. N. Fioretti, P. P. Zawadzki, L. T. Schelhas, E. S. Toberer, A. Zakutayev, and A. C. Tamboli, Phys. Rev. Mater. **1**, 035401 (2017).
[19] P. E. Blöchl, Phys. Rev. B **50**, 17953 (1994).
[20] G. Kresse and D. Joubert, Phys. Rev. B **59**, 1758 (1999).
[21] G. Kresse and J. Furthmüller, Phys. Rev. B **54**, 11169 (1996).
[22] A. V. Krukau, O. A. Vydrov, A. F. Izmaylov, and G. E. Scuseria, J. Chem. Phys. **125**, 224106 (2006).
[23] P. C. Quayle, K. He, J. Shan, and K. Kash, MRS Commun. **3**, 135 (2013).
[24] V. S. Olsen, V. Øversjøen, D. Gogova, B. Pécz, A. Galeckas, J. Borgersen, K. Karlsen, L. Vines, and A. Kuznetsov, Adv. Opt. Mater. **9**, 2100015 (2021).
[25] C. Freysoldt, B. Grabowski, T. Hickel, J. Neugebauer, G. Kresse, A. Janotti, and C. G. Van de Walle, Rev. Mod. Phys. **86**, 253 (2014).
[26] C. Freysoldt, J. Neugebauer, and C. G. Van de Walle, Phys. Rev. Lett. **102**, 016402 (2009).
[27] Y. Kumagai and F. Oba, Phys. Rev. B **89**, 195205 (2014).
[28] G. Henkelman, B. P. Uberuaga, and H. Jansson, J. Chem. Phys. **113**, 9901 (2000).
[29] J. Sun, A. Ruzsinszky, and J. P. Perdew, Phys. Rev. Lett. **115**, 036402 (2015).
[30] Y. K. Frodason, K. M. Johansen, A. Galeckas, and L. Vines, Phys. Rev. B **100**, 184102 (2019).
[31] S. Lany and A. Zunger, Appl. Phys. Lett. **96**, 142114 (2010).
[32] D. O. Demchenko, I. C. Diallo, and M. A. Reshchikov, Phys. Rev. B **97**, 205205 (2018).
[33] D. Steiauf, J. L. Lyons, A. Janotti, and C. G. Van de Walle, APL Mater. **2**, 096101 (2014).
[34] See Supplemental Material at http://link.aps.org/supplemental/10.1103/PhysRevMaterials.6.124602 for XRD survey scans for samples A–H, FTIR measurements exhibiting free-carrier absorption, and the stability of Li in $ZnSnN_2$ measured by SIMS.
[35] M. B. Tellekamp, A. Osella, K. N. Heinselman, A. C. Tamboli, and C. Ban, APL Mater. **10**, 041109 (2022).
[36] J. B. Yi, C. C. Lim, G. Z. Xing, H. M. Fan, L. H. Van, S. L. Huang, K. S. Yang, X. L. Huang, X. B. Qin, B. Y. Wang, T. Wu, L. Wang, H. T. Zhang, X. Y. Gao, T. Liu, A. T. S. Wee, Y. P. Feng, and J. Ding, Phys. Rev. Lett. **104**, 137201 (2010).
[37] D. Gogova, V. S. Olsen, C. Bazioti, I.-H. Lee, Ø. Prytz, L. Vines, and A. Y. Kuznetsov, CrystEngComm **22**, 6268 (2020).